Inorganic Chemistry
Article

Inorg. Chem. **2010**, *49*, 11619–11626 **11619**
DOI: 10.1021/ic102052r

Ordered Mesoporous MFe_2O_4 (M = Co, Cu, Mg, Ni, Zn) Thin Films with Nanocrystalline Walls, Uniform 16 nm Diameter Pores and High Thermal Stability: Template-Directed Synthesis and Characterization of Redox Active Trevorite

Jan Haetge, Christian Suchomski, and Torsten Brezesinski*

Institute of Physical Chemistry, Justus-Liebig-University Giessen, Heinrich-Buff Ring 58, Giessen 35392, Germany

Received October 11, 2010

In this paper, we report on ordered mesoporous $NiFe_2O_4$ thin films synthesized via co-assembly of hydrated ferric nitrate and nickel chloride with an amphiphilic diblock copolymer, referred to as KLE. We establish that the $NiFe_2O_4$ samples are highly crystalline after calcination at 600 °C, and that the conversion of the amorphous inorganic framework comes at little cost to the ordering of the high quality cubic network of pores averaging 16 nm in diameter. We further show that the synthesis method employed in this work can be readily extended to other ferrites, such as $CoFe_2O_4$, $CuFe_2O_4$, $MgFe_2O_4$, and $ZnFe_2O_4$, which could pave the way for innovative device design. While this article focuses on the self-assembly and characterization of these materials using various state-of-the-art techniques, including electron microscopy, grazing incidence small-angle X-ray scattering (GISAXS), time-of-flight secondary ion mass spectrometry (TOF-SIMS), X-ray photoelectron spectroscopy (XPS), as well as UV−vis and Raman spectroscopy, we also examine the electrochemical properties and show the benefits of combining a continuous mesoporosity with nanocrystalline films. KLE-templated $NiFe_2O_4$ electrodes exhibit reasonable levels of lithium ion storage at short charging times which stem from facile pseudocapacitance.

Introduction

In recent years, it has been shown that polymer and surfactant templating of inorganic materials can be used to produce composites with periodicities on the nanoscale.[1−4] The formation of these composite materials relies on the solution phase co-assembly of inorganic oligomers or preformed nanocrystalline building blocks with organic structure-directing agents to produce periodicities reminiscent of lyotropic liquid crystal phases.[5−7] Materials in film format can be produced by the same template-directed synthesis methods but using an evaporation-induced self-assembly (EISA) process.[8,9] This process has become widespread since Brinker and others published their seminal papers on patterned porous thin films in the late 1990s.

However, despite the fact that a broad range of inorganic compounds with ordered nanoscale porosity can be made, the majority of these templated materials do not allow the inorganic walls to be crystallized while retaining order. It has been shown, for example, that when mesoporous metal oxides with 3−6 nm thick walls are produced, whether in the form of films or powders, the nanoscale structure is not well preserved after crystallization and in most cases the porosity is ill-defined.[10,11] One reason for this is that the stable critical nucleation size is often larger than the inorganic walls themselves, which helps explain the loss of order at the onset of crystallization.

This work focuses on MFe_2O_4 (M = Co, Cu, Mg, Ni, Zn) thin films, and more specifically, on trevorite ($NiFe_2O_4$, NFO), a material that we show here how to synthesize with both a mesoporous morphology and nanocrystalline walls by utilizing a poly(ethylene-*co*-butylene)-*block*-poly(ethylene oxide) diblock copolymer, referred to as KLE,[12] as the

*To whom correspondence should be addressed. E-mail: torsten.brezesinski@phys.chemie.uni-giessen.de.

(1) Beck, J. S.; Vartuli, J. C.; Roth, W. J.; Leonowicz, M. E.; Kresge, C. T.; Schmitt, K. D.; Chu, C. T. W.; Olson, D. H.; Sheppard, E. W.; McCullen, S. B.; Higgins, J. B.; Schlenker, J. L. *J. Am. Chem. Soc.* **1992**, *114*, 10834.
(2) Mann, S. *Nat. Mater.* **2009**, *8*, 781.
(3) Goltner, C. G.; Antonietti, M. *Adv. Mater.* **1997**, *9*, 431.
(4) Ozin, G. A.; Hou, K.; Lotsch, B. V.; Cademartiri, L.; Puzzo, D. P.; Scotognella, F.; Ghadimi, A.; Thomson, J. *Mater. Today* **2009**, *12*, 12.
(5) Sanchez, C.; Boissiere, C.; Grosso, D.; Laberty, C.; Nicole, L. *Chem. Mater.* **2008**, *20*, 682.
(6) Corma, A.; Atienzar, P.; Garcia, H.; Chane-Ching, J. Y. *Nat. Mater.* **2004**, *3*, 394.
(7) Ba, J. H.; Polleux, J.; Antonietti, M.; Niederberger, M. *Adv. Mater.* **2005**, *17*, 2509.
(8) Ogawa, M. *Langmuir* **1997**, *13*, 1853.
(9) Brinker, C. J.; Lu, Y. F.; Sellinger, A.; Fan, H. Y. *Adv. Mater.* **1999**, *11*, 579.
(10) Li, D. L.; Zhou, H. S.; Honma, I. *Nat. Mater.* **2004**, *3*, 65.
(11) Richman, E. K.; Kang, C. B.; Brezesinski, T.; Tolbert, S. H. *Nano Lett.* **2008**, *8*, 3075.
(12) Thomas, A.; Schlaad, H.; Smarsly, B.; Antonietti, M. *Langmuir* **2003**, *19*, 4455.

Published on Web 11/18/2010

structure-directing agent. The advantage in using KLE over commercially available polymers, such as Pluronic type templates, is that KLE produces composites with 20−30 nm repeat distances. These large distances allow the walls to be sufficiently thick, which in turn allows for uniform nucleation and growth of the crystalline phase with retention of the periodicity.[13,14]

Ferrites, such as NFO, represent an important class of materials that are used extensively in the field of transformers, electronic inductors, magnetic memory and two phase multiferroics with strain mediated coupling.[15−17] Moreover, it has also been shown that ferrites with nanocrystalline grain structures are feasible materials for electrochemical charge storage, which can reversibly deliver up to 600 mAh/g in the potential range between 3 and 0.01 V versus Li/Li^+ despite their finite electronic resistance.[18−20] The importance of nanocrystallinity for achieving reasonable charge storage characteristics has been pointed out frequently. That is, even though ferrites are redox active oxides, bulk forms of these materials have not proven to be of much interest for battery applications because of modest reaction kinetics and poor cycling behavior (note that small particles can more easily accommodate the strains from lithium insertion compared to micrometer-sized particles).

The question then arises as to why porous versions of nanocrystalline ferrites may be beneficial in further improving their electrochemical potential. The advantages in using porous materials for high rate rechargeable lithium batteries are typically attributed to short diffusion path lengths for both electron and lithium ion transport.[21,22] In this paper, however, we show that the increased opportunity for charge storage from capacitive effects also accounts for the improved performance, in particular for the comparatively high levels of lithium ion storage at short charging times. That is, by creating porous versions of redox active compounds we expect to produce materials whose electrochemical properties are determined by surfaces and interfaces and not by bulk behavior.[23,24]

Capacitive energy storage is based on electrochemical capacitors, which include supercapacitors and pseudocapacitors, and is distinguished from other types of electrochemical energy storage by short charging times and the ability to deliver more power than batteries.[25−28] Non-faradaic processes, though, in which charge is stored electrostatically in a thin double-layer at the electrode/electrolyte interface, are not the focus here. Rather, faradaic charge-transfer mechanisms are of interest because the energy density associated with faradaic reactions is substantially larger.

This paper describes the soft-templating synthesis and characterization of ordered mesoporous NFO thin films. We then examine the ability of these materials to store charge with a specific focus on how the surface area can facilitate that charge storage. While the samples studied here do not break records for either energy or power density, our results offer insight into how continuous mesoporosity can be used to enhance charge storage in a material whose bulk form exhibits rather limited behavior.

Experimental Section

Materials. $Fe(NO_3)_3 \cdot 9H_2O$ (99.99%), $NiCl_2 \cdot 6H_2O$ (99.99%), and 2-methoxyethanol (99.8%) were purchased from Sigma-Aldrich. $H[(CH_2CH_2)_{0.67}(CH_2CHCH_2CH_3)_{0.33}]_{89}(OCH_2CH_2)_{79}OH$, referred to as KLE,[12] was used as the structure-directing agent.

Synthesis. In a small container, both 310.2 mg of $Fe(NO_3)_3 \cdot 9H_2O$ and 91.3 mg of $NiCl_2 \cdot 6H_2O$ dissolved in 1.8 mL of EtOH are combined with 40 mg of KLE dissolved in 0.6 mL of 2-methoxyethanol. After stirring the solution for 30 min, films can be produced via dip-coating on polar substrates including fluorine-doped SnO_2 (FTO) glass and (100)-oriented silicon wafers. Optimal conditions include relative humidities below 10% and constant withdrawal rates of 1−10 mm/s. For best results, the films are aged at 250 °C for 12 h and then calcined in air using a 45 min ramp to 600 °C followed by a 5−10 min soak.

Characterization. Bright-field transmission electron microscope (TEM) and scanning electron microscope (SEM) images were taken with a CM30-ST microscope from Philips and a LEO GEMINI 982, respectively. Tapping mode atomic force microscope (AFM) images were collected on a multimode AFM from Veeco Instruments employing Olympus microcantilevers (resonance frequency: 300 kHz, force constant: 42 N/m). Wide-angle X-ray scattering (WAXS) measurements were carried out on an X'Pert PRO diffractometer from PANalytical instruments utilizing a Θ-2Θ geometry. GISAXS data were collected at the German synchrotron radiation facility HASYLAB/DESY on beamline BW4 using a MarCCD area detector and a sample−detector distance of 1820 mm. X-ray photoelectron spectroscopy (XPS) spectra were acquired on a Physical Electronics ESCA 5600 spectrometer with monochromatic $Al-K_\alpha$ X-ray source (P = 200 W) and multichannel detector OmniIV. The electron takeoff angle to the sample surface was adjusted to 45°. The C1s signal from adventitious hydrocarbon at 284.6 eV was used as the energy reference to correct for charging. Raman spectra were acquired using the SENTERRA dispersive Raman microscope from Bruker Optics equipped with an objective from Olympus (MPlan N 20x, FN = 22, NA = 0.40) and a Nd:YAG laser (λ = 532 nm, P = 10 mW). The samples were also analyzed by time-of-flight secondary ion mass spectrometry using a TOF-SIMS 5 from ION-TOF GmbH. A beam of 25 keV Bi^+ focused to a 60 μm spot was used to generate secondary ions for analysis. Sputter etching was carried out using a beam of 1 keV O^+ (I_O = 131.1 nA) focused to a 170 μm spot. Krypton physisorption measurements were conducted at 87 K on 120 nm thick NFO films with a total area of ~38 cm^2 using the Autosorb-1-MP automated gas adsorption station from Quantachrome Corporation. Optical absorption measurements were

(13) Brezesinski, K.; Ostermann, R.; Hartmann, P.; Perlich, J.; Brezesinski, T. *Chem. Mater.* **2010**, *22*, 3079.
(14) Brezesinski, T.; Wang, J.; Senter, R.; Brezesinski, K.; Dunn, B.; Tolbert, S. H. *ACS Nano* **2010**, *4*, 967.
(15) Zhai, J. Y.; Cai, N.; Shi, Z.; Lin, Y. H.; Nan, C. W. *J. Appl. Phys.* **2004**, *95*, 5685.
(16) Liu, M.; Li, X.; Imrane, H.; Chen, Y. J.; Goodrich, T.; Cai, Z. H.; Ziemer, K. S.; Huang, J. Y.; Sun, N. X. *Appl. Phys. Lett.* **2007**, *90*, 152501.
(17) Deng, C. Y.; Zhang, Y.; Ma, J.; Lin, Y. H.; Nan, C. W. *Acta Mater.* **2008**, *56*, 405.
(18) Bomio, M.; Lavela, P.; Tirado, J. L. *ChemPhysChem* **2007**, *8*, 1999.
(19) Vidal-Abarca, C.; Lavela, P.; Tirado, J. L. *Solid State Ionics* **2010**, *181*, 616.
(20) Lavela, P.; Tirado, J. L. *J. Power Sources* **2007**, *172*, 379.
(21) Wilkening, M.; Lyness, C.; Armstrong, A. R.; Bruce, P. G. *J. Phys. Chem. C* **2009**, *113*, 4741.
(22) Jamnik, J.; Maier, J. *Phys. Chem. Chem. Phys.* **2003**, *5*, 5215.
(23) Grosso, D.; Boissiere, C.; Smarsly, B.; Brezesinski, T.; Pinna, N.; Albouy, P. A.; Amenitsch, H.; Antonietti, M.; Sanchez, C. *Nat. Mater.* **2004**, *3*, 787.
(24) Arico, A. S.; Bruce, P.; Scrosati, B.; Tarascon, J. M.; Van Schalkwijk, W. *Nat. Mater.* **2005**, *4*, 366–377.
(25) Winter, M.; Brodd, R. *J. Chem. Rev.* **2004**, *104*, 4245.
(26) Conway, B. E. *Electrochemical Supercapacitors*; Kluwer Academic: New York, 1999.
(27) Zheng, J. P.; Huang, J.; Jow, T. R. *J. Electrochem. Soc.* **1997**, *144*, 2026.
(28) Conway, B. E.; Birss, V.; Wojtowicz, J. *J. Power Sources* **1997**, *66*, 1.

carried out on a PERKIN ELMER Lambda 900 UV−vis−NIR spectrophotometer. A substrate made from fused silica and an aluminum mirror served as the reference for transmission and reflection measurements, respectively. The film thickness was determined with an Alpha Step IQ Surface Profiler from KLA Tencor.

Electrochemical experiments were carried out in an argon filled glovebox in a three-electrode cell using an Autolab PGSTAT302 potentiostat. A lithium foil several times the area of the working electrode was used as the counter electrode; the reference electrode was a lithium wire. The electrolyte solution was 1.0 M $LiClO_4$ in propylene carbonate (PC). Cyclic voltammetry was used to study the electrochemical behavior using cutoff voltages at 3.50 and 1.45 V versus Li/Li^+. For the double layer capacitance experiments, the electrolyte was changed to 1.0 M tetrabutylammonium (TBA^+) perchlorate in PC. The loading of the films varied from approximately 50 to 100 $\mu g/cm^2$. The weight was calculated by directly measuring the thickness and porosity and knowing the density of the trevorite phase. We estimate the error as being ±5%.

Results and Discussion

Many methods, including electrodeposition, electrospinning, and various sol gel techniques have been utilized to produce nanocrystalline NFO materials in forms other than bulk.[29−31] The use of EISA to produce NFO thin films with controlled nanoscale periodicity, however, has not been reported so far.

Briefly, an isotropic solution made from ethanol, 2-methoxyethanol, and KLE as well as hydrated ferric nitrate and nickel chloride is dip-coated onto a polar substrate. On evaporation of the volatile constituents, the system co-assembles to form an inorganic/organic composite with long-range nanoscale periodicity. Thermal treatment can be used to further cross-link the inorganic framework and remove the organic template, producing a 3-dimensional mesoporous architecture as described below.

The use of 2-methoxyethanol as a co-solvent is not crucial for a successful synthesis. We find, however, that it slows down the drying time of the KLE-templated thin films, which in turn leads to more homogeneous and better ordered materials. Also, the addition of 2-methoxyethanol improves the stability of the dip-coating solution simply because the KLE diblock copolymer is more readily soluble in 2-methoxyethanol than in ethanol. At this point we note again that one reason for using KLE (made by polymerization of ethylene oxide using "Kraton Liquid" as macroinitiator)[12] rather than Pluronic type templates, such as P123 or F127, is that this structure-directing agent has been shown to be highly suitable for the synthesis of oxide materials with both a mesoporous morphology and nanocrystalline walls.[32] Also, we find that the same syntheses employed here failed when using Pluronic type templates, a result that further underscores the superior templating properties of KLE.

To our knowledge, this is the first work to report the template-directed synthesis of ordered mesoporous NFO (as well as of $CuFe_2O_4$, $MgFe_2O_4$, and $ZnFe_2O_4$) nanoarchitectures with highly crystalline walls in the form of thin films.

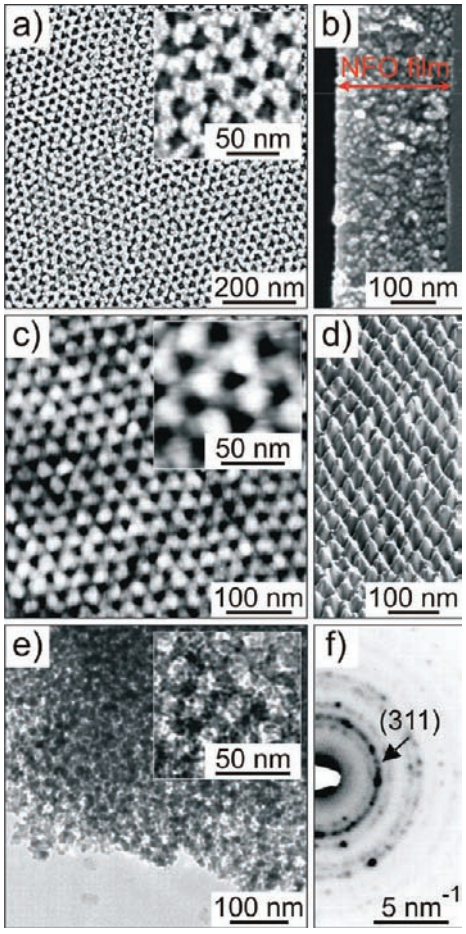

Figure 1. Morphology of ~250 nm thick KLE-templated NFO films calcined at 600 °C. (a) Top view SEM image showing open pores at the sample/air interface. The inset in (a) is a high-magnification SEM image. (b) Cross-sectional SEM image; the film was sputtered with ~0.5 nm Pt prior to imaging. (c) Tapping mode AFM height image showing the hexagonal top surface. The inset in (c) is a high-magnification AFM image. (d) 3D-AFM height image at a tilt of 60°. (e) Bright-field TEM image showing that the periodic structure observed at the top surface persists throughout the bulk of the films. The inset in (e) is a high-magnification TEM image. (f) Selected area electron diffraction pattern of the same sample shown in (e).

The synthesis and magnetic properties of KLE-templated $CoFe_2O_4$ have been reported previously.[33] However, some of the ferrites discussed here have already been prepared in powder form by confined growth inside a rigid material, such as SBA-15 or KIT-6.[34−37] In general, however, these so-called hard-templating or nanocasting routes suffer from time-consuming processing steps and poor control over the overall material homogeneity. In addition, they involve the use of base or acid to remove the mold in case a siliceous material served as the hard template, a treatment that can have a negative effect on material properties.

(29) NuLi, Y. N.; Qin, Q. Z. *J. Power Sources* **2005**, *142*, 292.
(30) Chen, D. H.; He, X. R. *Mater. Res. Bull.* **2001**, *36*, 1369.
(31) Jiang, J.; Yang, Y. M. *Mater. Lett.* **2007**, *61*, 4276.
(32) Brezesinski, K.; Wang, J.; Haetge, J.; Reitz, C.; Steinmueller, S. O.; Tolbert, S. H.; Smarsly, B. M.; Dunn, B.; Brezesinski, T. *J. Am. Chem. Soc.* **2010**, *132*, 6982.
(33) Quickel, T. E.; Le, V. H.; Brezesinski, T.; Tolbert, S. H. *Nano Lett.* **2010**, *10*, 2982.
(34) Sun, Y. Y.; Ji, G. B.; Zheng, M. B.; Chang, X. F.; Li, S. D.; Zhang, Y. *J. Mater. Chem.* **2010**, *20*, 945.
(35) Gu, M.; Yue, B.; Bao, R. L.; He, H. Y. *Mater. Res. Bull.* **2009**, *44*, 1422.
(36) El-Sheikh, S. H.; Harraz, F. A.; Hessien, M. M. *Mater. Chem. Phys.* **2010**, *123*, 254.
(37) Valdes-Solis, T.; Tartaj, P.; Marban, G.; Fuertes, A. B. *Nanotechnology* **2007**, *18*, 145603.
(38) Sel, O.; Sallard, S.; Brezesinski, T.; Rathousky, J.; Dunphy, D. R.; Collord, A.; Smarsly, B. M. *Adv. Funct. Mater.* **2007**, *17*, 3241.

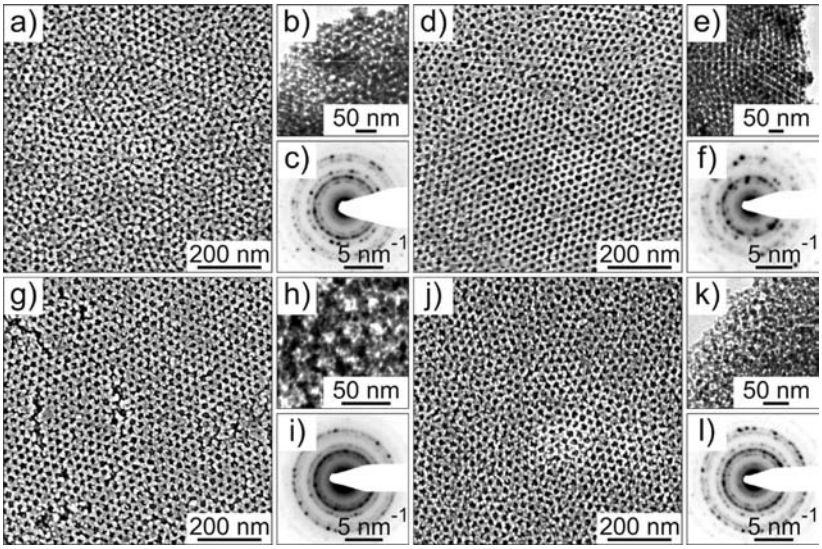

Figure 2. Morphology of KLE-templated $CoFe_2O_4$ (a−c), $CuFe_2O_4$ (d−f), $MgFe_2O_4$ (g−i), and $ZnFe_2O_4$ (j−l) thin films calcined at 650, 625, 650, and 550 °C, respectively. (a,d,g,j) SEM images of the various top surfaces. (b,e,h,k) Bright-field TEM images showing that the cubic pore structures persist throughout the films. (c,f,i,l) Selected area electron diffraction patterns characteristic of nanocrystalline materials with randomly oriented domain structures. It is evident from these patterns that the films are composed of cubic $CoFe_2O_4$, tetragonal $CuFe_2O_4$, cubic $MgFe_2O_4$, and cubic $ZnFe_2O_4$ as corroborated by JCPDS reference cards no. 22-1086, 34-0425, 36-0398, and 22-1012, respectively.

Figures 1a−e show SEM, TEM, and AFM images of ~250 nm thick NFO films after removal of the KLE template and crystallization of the inorganic material at 600 °C. Both the top view SEM and tapping mode AFM height images reveal a high quality cubic network of pores averaging 16 nm in diameter. It is evident from these images that the self-assembled NFO thin films are both homogeneous and crack-free at the micrometer length scale (see also Supporting Information, Figure S1). In addition, it can be seen that the pores at the sample/air interface are open. This result is important since the absence of a sealing layer at the top surface is a basic requirement for the fabrication of composite materials, such as two phase multiferroics (piezoelectric-magnetostrictive composites). The hexagonal top surface is also very flat with a root-mean-square (rms) roughness of less than 1 nm. From cross-sectional SEM and bright-field TEM we are able to establish that the periodic structure persists throughout the films. Figure 1f is an electron diffraction pattern showing Debye−Scherrer rings characteristic of a nanocrystalline material with randomly oriented domains. Calculated lattice spacings are in agreement with JCPDS reference card no. 10-0325 and show the film to be composed of inverse spinel trevorite in phase pure form.

Both Brunauer−Emmett−Teller (BET) surface area and porosity were determined by krypton physisorption measurements. Full adsorption/desorption isotherms could not be collected at 77 K, however. The reason for this failure is presumably due to the gas−solid transition in the large pores at 77 K. Measurements at 87 K, by contrast, allowed for a proper gas−liquid transition. Using a saturation pressure of 13 Torr and a cross-sectional area of 20.5 Å for Kr, a BET surface area of 180 m^2/cm^3 and a pore volume of 1.28×10^{-4} cm^3 (equivalent to 28% porosity) are obtained for NFO thin films calcined at 600 °C. These values are characteristic of metal oxides templated with the diblock copolymer KLE.

Figures 2a-l show electron microscope images and diffraction patterns of KLE-templated $CoFe_2O_4$, $CuFe_2O_4$, $MgFe_2O_4$, and $ZnFe_2O_4$ thin films calcined at 650, 625, 650, and 550 °C, respectively. These data indicate that the synthesis method employed in this work can be readily extended to other ferrite materials, which could pave the way for innovative device design. Both the top view SEM and bright-field TEM images reveal ordered cubic networks of open pores. Similar to that of NFO, the samples are homogeneous, that is, with no major structural defects at the micrometer level, and exhibit pore walls that are composed of randomly oriented crystallites. A more detailed characterization of these KLE-templated materials will be shown in a separate work.

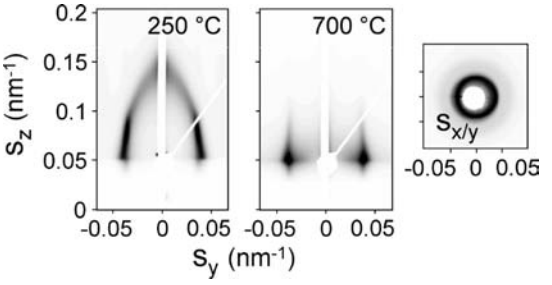

Figure 3. Synchrotron-based SAXS on KLE-templated NFO thin films with amorphous (250 °C) and nanocrystalline (700 °C) pore walls. The GISAXS patterns were collected at an angle of incidence $\beta = 0.2°$ and show the evolution of the distorted cubic pore network upon thermal treatment. A SAXS pattern in transmission mode, that is, at $\beta = 90°$, of the sample heated to 700 °C is shown on the right. Scattering vector, $\boldsymbol{s}$, components are given in nm^{-1}.

Overall, the data in Figures 1 and 2 collectively establish that high quality ferrite thin films can be readily produced by a facile soft solution-processing route using KLE as the structure-directing agent. Moreover, they suggest that the mesoporous morphology of the various ferrite materials is well retained when the crystalline phase is achieved.

More quantitative information on the structure of the KLE-templated NFO thin films was obtained using grazing incidence small-angle X-ray scattering (GISAXS) and conventional SAXS. Figure 3 shows GISAXS patterns collected at an angle of incidence $\beta = 0.2°$. It can be seen that

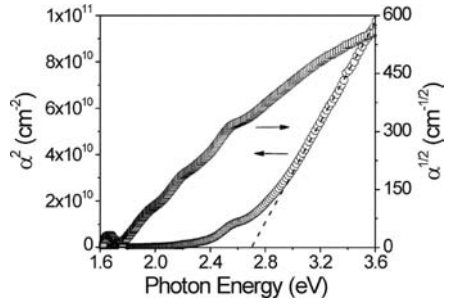

Figure 4. Plots for both direct (○) and indirect (□) optical transitions in KLE-templated NFO thin films calcined at 600 °C.

amorphous samples (250 °C) produce patterns with distinct scattering maxima. These maxima, however, cannot be clearly indexed to a certain cubic phase. We note that KLE-templated materials typically show either a face-centered-cubic close-packed structure with (111) orientation relative to the plane of the substrate or a body-centered-cubic *Im3m*-derived structure.[14,32,38] For NFO, the latter seems to be less likely considering the hexagonal symmetry of the top surface (see Figure 1). Since no conclusions about the orientation seem possible on the basis of the data presented here, we refer to the structure as a distorted cubic pore network. It can also be seen in Figure 3 that samples heated to 700 °C have lost their out-of-plane periodicity. The reason for the lack of out-of-plane scattering is that the crystallization process is accompanied by a slight restructuring of the pore network. Since these films have only 10 to 15 repeat units in the direction normal to the substrate, this restructuring has a greater effect on the out-of-plane periodicity.

The GISAXS patterns further indicate a large lattice contraction perpendicular to the plane of the substrate. The in-plane contraction, by contrast, is negligible as the materials are pinned to the substrate. On the basis of the relative position of the out-of-plane scattering maxima of samples heated to 250 °C (the in-plane *d*-spacing is ~26 nm), we estimate the decrease in inorganic volume as being approximately 75%. Higher annealing temperatures do not lead to further contraction as the ligands of both inorganic precursors are fully decomposed by 250 °C. This result is in agreement with both the SAXS data shown in Supporting Information, Figure S2 and previous studies on the thermal decomposition of hydrated ferric nitrate.[39,40]

Lastly, Figure 3 also shows a small-angle X-ray scattering (SAXS) pattern in transmission mode of the sample heated to 700 °C. This pattern provides ample evidence for the retention of in-plane pore ordering after crystallization of the amorphous inorganic framework. We conclude from this data that (1) NFO effectively withstands the stress generated during thermal treatment and that (2) no distinct restructuring of the distorted cubic pore network occurs upon crystallization. That is, the pore-solid architectures studied here can readily accommodate the trevorite crystallites that form at the onset of crystallization.

Supporting Information, Figure S2 shows conventional SAXS data (Bragg−Brentano geometry), which further support the structure and morphology results. In contrast to the

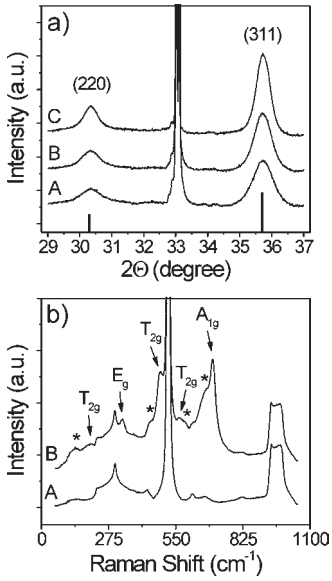

Figure 5. (a) WAXS patterns obtained on KLE-templated NFO thin films heated to 600 (A), 650 (B), and 700 (C) °C. The peaks at 2Θ = 33° and 34° can be attributed to silicon and spurious background peaks, respectively. The line pattern shows JCPDS reference card no. 10-0325 for cubic trevorite. (b) Raman spectra obtained on a bare (100)-oriented silicon substrate (A) and a 250 nm thick KLE-templated NFO film (B). The asterisks indicate Raman modes that are not observed in defect-free NFO with purely inverse spinel structure.

GISAXS patterns in Figure 3, these scans provide only information on the out-of-plane periodicity. The fact that even a distinct second order reflection can be observed for amorphous samples despite being in thin film form underlines the high degree of pore ordering.

Apart from the typical scope of ferrite materials, it is envisioned to exploit their interesting optical properties, for example, in visible-light photoactive composites or magneto-optical devices. For such applications, knowledge of the band gap energy is crucial. The following equation can be used to describe the dependence of absorption coefficient, α, on the difference between the photon energy of incident light, $h\nu$, and the band gap energy, E_g (with $h\nu > E_g$):

$$\alpha \propto (h\nu - E_g)^n \quad (1)$$

In eq 1, n represents the type of optical transition. For $n = 1/2$, this transition is direct while $n = 2$ indicates an indirect optical transition. Figure 4 shows plots for both transitions. However, the lack of the characteristic shape of the plot, $\alpha^{1/2}$ versus photon energy, argues against an indirect optical transition in KLE-templated NFO thin films calcined at 600 °C. In contrast, the plot for the direct transition reveals the expected shape, and extrapolation of the linear part of the curve to zero provides an optical band gap at 2.7 eV (equivalent to 460 nm light). This result is in agreement with reported measured values for NFO materials.[41,42]

Lastly, a series of WAXS, Raman spectroscopy, XPS, and time-of-flight secondary ion mass spectrometry (TOF-SIMS) measurements were carried out to provide insight into the crystallization behavior of the films, their elemental composition, and whether impurity phases are present.

(39) Cseri, T.; Bekassy, S.; Kenessey, G.; Liptay, G.; Figueras, F. *Thermochim. Acta* **1996**, *288*, 137.
(40) Stefanescu, M.; Stefanescu, O.; Stoia, M.; Lazau, C. *J. Therm. Anal. Calorim.* **2007**, *88*, 27.
(41) Dolia, S. N.; Sharma, R.; Sharma, M. P.; Saxena, N. S. *Indian J. Pure Appl. Phys.* **2006**, *44*, 774.
(42) Balaji, S.; Selvan, R. K.; Berchmans, L. J.; Angappan, S.; Subramanian, K.; Augustin, C. O. *Mater. Sci. Eng., B* **2005**, *119*, 119.

Figure 5a shows WAXS data obtained on samples heated to various annealing temperatures, which establish that all characteristics of the self-assembled NFO thin films can be associated with the desired trevorite phase. Neither pattern shows the presence of second phases, such as goethite (α-FeOOH), hematite (α-Fe_2O_3), maghemite (γ-Fe_2O_3), or magnetite (Fe_3O_4), which could potentially be formed during thermal treatment because of the presence of iron-rich regions. The crystallization occurs at around 600 °C (at a heating rate of 10 °C/min). Applying the Scherrer equation to the full width at half-maximum intensity of the (311) peak gives an average crystallite size of 9 nm. This domain size, however, can be tuned up to approximately 16 nm while retaining nanoscale structure. Extensive domain growth because of sintering of trevorite grains is observed at annealing temperatures above 700 °C. This growth is associated with the loss of nanoscale periodicity. If the initial domain size of 9 nm is assumed to be the stable critical nucleation size, this provides a hypothesis for understanding why the same synthesis using Pluronic type templates failed. Stable nuclei smaller than the pore walls should allow for uniform nucleation and growth of the crystalline phase with retention of the periodicity, which is the case for KLE-templated NFO. If larger nuclei are present at the onset of crystallization, more restructuring of the pore network is likely to occur.[11]

Since conventional X-ray scattering techniques can be insensitive to poorly crystalline materials and small amounts of second phases as well as lattice distortions and dislocations, Raman measurements were also carried out. According to group theory, inverse spinel trevorite has 5 Raman-active phonon modes, namely, $1A_{1g}$, $1E_g$, and $3T_{2g}$ (or alternatively $3F_{2g}$).[43] Surprisingly, there is no superposition of the spectrum from the silicon substrate and thus all of the aforementioned Raman modes can be observed at 206, 331, 487, 565, and 700 cm^{-1} in Figure 5b. In addition to these bands, however, we find 4 more at 142, 450, 587, and 670 cm^{-1} which are not allowed in defect-free NFO with purely inverse spinel structure. The appearance of a distinct band at ~670 cm^{-1} is often associated with the formation of Fe_3O_4.[44] This, however, is chemically unreasonable as it would imply that some of the Fe^{3+} ions are reduced despite high temperature calcination. Also, XPS (see Figure 6a) does not indicate the presence of Fe^{2+}. Taking into account the sensitivity of the different techniques used in this work, we conclude that the amount of Fe_3O_4 and other impurity phases in the KLE-templated NFO thin films is less than 1%.

The question then arises as to why we observe these extra bands, and there seem to be at least two possible explanations. First, it has been shown that short-range ordering of the Fe^{3+} and Ni^{2+} ions on the octahedral sites leads to the formation of domains with lower microscopic symmetry,[45] which in turn may lead to the appearance of new Raman modes. Second, it is possible that there is a random Ni^{2+} distribution among the tetrahedral (^{iv}) and octahedral (^{vi}) sites, which may also lead to additional bands.[46]

The cation distribution is typically analyzed in terms of the inversion parameter, x, with $\{^{iv}[M_{1-x}Fe_x]^{vi}[M_xFe_{2-x}]O_4\}$. The two ordered configurations with $x = 0$ (normal spinel) and $x = 1$ (inverse spinel) are commonly observed for $ZnFe_2O_4$ and $NiFe_2O_4$, respectively, whereas other ferrites, such as $MgFe_2O_4$ exhibit a random distribution. From a chemical point of view, however, it is reasonable to expect a lower degree of cation ordering, simply because the self-assembled NFO thin films are both solution processed via sol−gel methods and nanocrystalline; thus they should contain some defects.

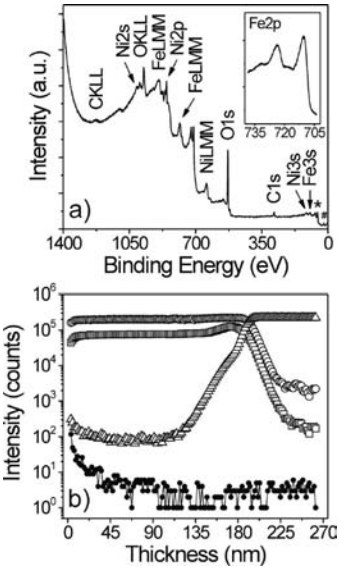

Figure 6. (a) Typical XPS survey spectrum for KLE-templated NFO thin films calcined at 600 °C. The Ni3p/Fe3p and O2s regions are indicated by (*) and (#), respectively. A high-resolution scan of the Fe2p core level is shown in the inset. (b) TOF-SIMS depth profile of a thin film on (100)-oriented silicon wafer showing the distribution of Fe^+ (○), Ni^+ (□), Si^+ (△), and C^+ (●).

Figure 6a shows a typical XPS survey spectrum for KLE-templated NFO thin films calcined at 600 °C in air. Apart from a very weak C1s peak, which we associate with adventitious hydrocarbon, only nickel, iron, and oxygen core levels are observed. Figure 6a further shows a high-resolution scan of the Fe2p region, which consists of a single doublet due to spin orbit splitting. The slight asymmetry of the $p_{1/2}$ and $p_{3/2}$ lines toward higher binding energy is due to Fe^{3+} occupying both tetrahedral and octahedral sites. The $p_{3/2}$ line can be fit to two mixed Gaussian/Lorentzian peaks (assuming Shirley background) at 709.74 ± 0.04 eV and 711.55 ± 0.04 eV in accordance with $^{vi}[Fe^{3+}]$ and $^{iv}[Fe^{3+}]$.[47] More importantly, the Fe2p region does not indicate the presence of Fe^{2+}. This result is further supported by the appearance of satellite peaks about 8 eV higher in binding energy than the main peaks. Such satellite structures are characteristic of iron being in the oxidation state 3+ rather than 2+ (note that Fe^{3+} is the stable oxidation state of iron under the experimental conditions).

The TOF-SIMS spectrum of a ~180 nm thick KLE-templated NFO film with nanocrystalline walls on (110)-oriented silicon wafer in Figure 6b illustrates the distribution of Fe^+ (○), Ni^+ (□), Si^+ (△), and C^+ (●) as a function of depth from the surface. This spectrum demonstrates that both Ni^{2+} and Fe^{3+} ions are homogeneously distributed throughout the films. The slow growth of the Ni^+ signal intensity near the

(43) White, W. B.; De Angelis, B. A. *Spectrochim. Acta* **1967**, *23A*, 985.
(44) Shebanova, O. N.; Lazor, P. *J. Solid State Chem.* **2003**, *174*, 424.
(45) Ivanov, V. G.; Abrashev, M. V.; Iliev, M. N.; Gospodinov, M. M.; Meen, J.; Aroyo, M. I. *Phys. Rev. B* **2010**, *82*, 024104.
(46) Jacob, J.; Khadar, M. A. *J. Appl. Phys.* **2010**, *107*, 114310.
(47) Zhang, J. L.; Shi, J. X.; Gong, M. L. *J. Solid State Chem.* **2009**, *182*, 2135.

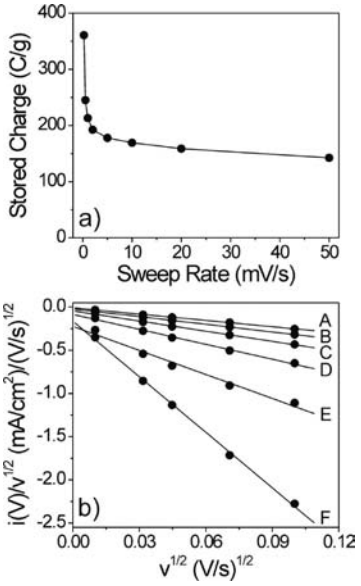

Figure 7. (a) Comparison of charging rates calculated from cyclic voltammetric data at various sweep rates. (b) Sweep rate dependence of the cathodic current for fixed potentials; (A) 2.5, (B) 2.3, (C) 2.1, (D) 1.9, (E) 1.7 and (F) 1.5 V versus Li/Li^+.

sample/substrate interface does not necessarily imply that nickel is enriched at this interface but rather indicates a different local environment. The chemical environment is known to have a significant impact on the ionization probability. This conclusion is further verified by the fact that, for example, potassium (K^+), which is always found as trace impurity, shows the same trend. Moreover, it is also evident from the data in Figure 6b that the KLE template is in fact removed throughout the films. Only minor amounts of hydrocarbons can be detected at the sample/air interface, which is consistent with the XPS result. The fact that the C^+ signal intensity begins to increase at a depth of ~100 nm already can be attributed to sputter induced ion mixing, which is typical of TOF-SIMS.

To examine the redox processes present in KLE-templated NFO with nanocrystalline walls, solution based voltammetry experiments were conducted on thin film electrodes using cutoff voltages at 3.50 and 1.45 V versus Li/Li^+. We did not investigate lower potentials because of concerns about electrolyte stability. Figure 7a shows a comparison of charging rates calculated from cyclic voltammetric data, which provides insight on the reaction kinetics. It can be clearly seen that the total amount of charge stored is strongly dependent upon charging time. This dependency not only implies the presence of kinetic limitations associated with the diffusion of lithium through the bulk of films but also suggests that different charge storage processes occur at different time scales.

At this point we note again that capacitive energy storage in microcrystalline materials is hindered by (1) slow electronic and lithium ion transport through the materials and (2) low surface areas. Creating nanostructured versions of redox active materials can thus can be a viable direction for energy storage applications because of the small crystalline domain sizes of such materials and the ability to access both bulk and surface redox sites.[14,24,32]

Regardless of the kinetic limitation, the mesoporous NFO thin film electrodes are capable of storing up to 145 C/g after

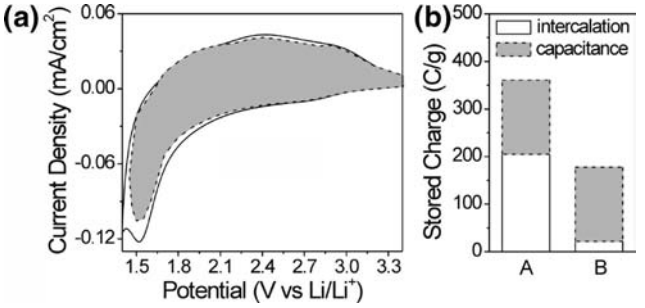

Figure 8. (a) Voltammetric sweep at 5 mV/s rate. The capacitive contribution to the total current is shown by the shaded region. (b) Comparison of the total stored charge. Approximately 90% of the total charge is capacitive at a sweep rate of 5 mV/s (B) while only 45% is capacitive in nature at 0.1 mV/s (A).

a charging time of only 40 s, which accounts for more than one-third of the total charge that is stored at a sweep rate of 0.1 mV/s, that is, at a charging time of ~20000 s. The only explanation for this result is a contribution from capacitive effects while diffusion-controlled lithium intercalation contributes at longer times.

The total stored charge can be separated into three components: (1) the faradaic contribution from Li^+ intercalation, (2) the faradaic contribution from charge-transfer processes with surface atoms, referred to as pseudocapacitive effect, and (3) the non-faradaic contribution from the double layer effect.

Following a previously reported approach by Lindstrom and Dunn et al., we are able to use the voltammetric sweep rate dependence to quantitatively distinguish the capacitive contribution to the current response.[48,49] The current response at a fixed potential is the combination of surface capacitive effects and diffusion-controlled Li^+ intercalation according to:

$$i(V) = k_1 v + k_2 v^{1/2} \quad (2)$$

with the measured current $i(V)$ at a fixed potential and the sweep rate v.[50] Equation 2 has two unknowns, namely, k_1 and k_2. To solve for both of these unknowns, $i(V)/v^{1/2}$ is plotted versus $v^{1/2}$ (see Figure 7b). By so doing, we have the ability to distinguish between the currents arising from diffusion-controlled intercalation processes and those from capacitive effects.

Figure 8a shows cyclic voltammetric data collected on a KLE-templated NFO thin film electrode after 5 cycles when the charge storage capacity had leveled off. It is apparent from this data that the samples studied in this work exhibit redox peaks at ~1.52 (cathodic) as well as 2.40 and 3.00 (anodic) V versus Li/Li^+, which have not been observed for conventional NFO materials. This result, therefore, suggests that the mesoporous NFO thin film electrodes have distinct intercalation sites that are not available to NFO in bulk form. However, it has been shown recently for nanocrystalline $ZnFe_2O_4$ that the cathodic peak can be attributed to the topotactic intercalation of lithium ions into the cubic lattice, that is, transformation of $ZnFe_2O_4$ to $Li_xZnFe_2O_4$.[51]

(48) Lindstrom, H.; Sodergren, S.; Solbrand, A.; Rensmo, H.; Hjelm, J.; Hagfeldt, A.; Lindquist, S. E. *J. Phys. Chem. B* **1997**, *101*, 7717.
(49) Wang, J.; Polleux, J.; Lim, J.; Dunn, B. *J. Phys. Chem. C* **2007**, *111*, 14925.
(50) Liu, T. C.; Pell, W. G.; Conway, B. E.; Roberson, S. L. *J. Electrochem. Soc.* **1998**, *145*, 1882.
(51) Guo, X. W.; Lu, X.; Fang, X. P.; Mao, Y.; Wang, Z. X.; Chen, L. Q.; Xu, X. X.; Yang, H.; Liu, Y. N. *Electrochem. Commun.* **2010**, *12*, 847.

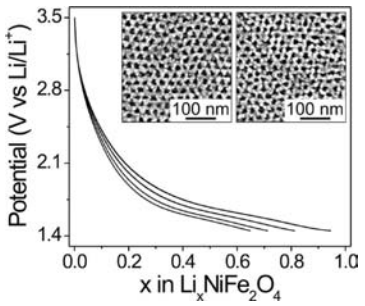

Figure 9. Galvanostatic discharge curves obtained at 3C (60 μA/cm^2), 2C (40 μA/cm^2), 1C (20 μA/cm^2), and C/2 (10 μA/cm^2) rates after the charge capacity had reached stable values. Insets show SEM images of the top surface of a KLE-templated NFO thin film electrode before and after galvanostatic cycling (100 cycles at 1C).

The area under the cyclic voltammetric curve represents the total amount of stored charge, which is divided into insertion capacity and capacitive charge storage. We find that some 90% of the total charge stored arises from capacitive effects. At a sweep rate of 0.1 mV/s, by contrast, only about 45% is capacitive in nature (see Figure 8b). The reason for this decrease is that longer charging time enables more current to be contributed from diffusion-controlled Li^+ intercalation processes. We note that the NFO samples employed here have effectively achieved their maximum capacitive contribution of ~155 C/g after a charging time of only 1 min.

This data, however, does not tell us whether the capacitive charge storage is related to double-layer or pseudocapacitive effects. While the nanocrystalline NFO thin film electrodes evidently do not set new records for high levels of energy or power density, this is an important question to be resolved if we are to take advantage of the faradaic processes occurring with these materials.

To separate the double layer capacitance from pseudocapacitance, separate voltammetry experiments were carried by using tetrabutylammonium (TBA^+) perchlorate in propylene carbonate as the electrolyte. The total charge storage shown in Figure 7a includes double layer capacitance, which can be readily observed using TBA^+, as well as pseudocapacitance and diffusion-controlled intercalation processes, which are based on using Li^+ electrolytes. We note that the bulky cation, TBA^+, can neither be intercalated into the trevorite lattice nor carry out charge-transfer reactions with surface atoms.

By examining voltammetric sweeps at 25 mV/s (Supporting Information, Figure S3), a rate which does not allow much time for charge storage by lithium intercalation, we find that the charge storage is largely from pseudocapacitance. That is, capacitive processes contribute to charge storage at short times while diffusion-controlled lithium intercalation contributes at longer times.

These conclusions are further verified by galvanostatic control experiments. Figure 9 shows discharge curves obtained on KLE-templated NFO thin film electrodes at 3C, 2C, 1C, and C/2 rates (1C is defined as 1 Li^+ per formula unit in 1 h at 25 °C). It can be clearly seen that the various voltage profiles reveal a subtle plateau at ~1.5 V. This plateau is in the range observed potentiostatically and is more pronounced at the slower rates (greater contribution from Li^+ intercalation), which is in agreement with the data shown in Figure 8. In addition, we find that the shape of the galvanostatic discharge curves does not change with cycle number and that cycling does neither lead to severe restructuring of the pore network nor to the appearance of cracks at the micrometer length scale (see SEM images in Figure 9 and Supporting Information, Figure S4). These results support the hypothesis of a topotactic intercalation.

As mentioned above, previous work has shown that the mole fraction of inserted lithium, x, over a similar potential range is some 0.5 for nanoscale $ZnFe_2O_4$.[51] The chemically related materials studied in this work are able to reversibly accommodate up to 0.95 Li^+ per formula unit at C/2. Moreover, they are also able to maintain stable cycling performance at rates as high as 3C with a mole fraction of inserted lithium of 0.65. This result demonstrates that the introduction of well-defined porosity with large surface area provides a beneficial microstructure for lithium insertion/extraction because of the ability to access both bulk (i.e., topotactic intercalation) and surface sites.

Conclusions

In this work, we have shown that $NiFe_2O_4$ can be templated using the diblock copolymer KLE to produce high quality thin film materials with both a mesoporous morphology and nanocrystalline walls. Moreover, we have also shown that the same template-directed synthesis method can be readily extended to other ferrites, such as $CoFe_2O_4$, $CuFe_2O_4$, $MgFe_2O_4$, and $ZnFe_2O_4$.

The results with electron microscopy, X-ray scattering, TOF-SIMS, XPS, and Raman spectroscopy demonstrate that the nanocrystalline $NiFe_2O_4$ thin films are homogeneous at the microscopic length scale and that they contain some defects at the atomic level. The reason that the amorphous inorganic pore wall structure can be fully crystallized while retaining nanoscale order is due to both the large domain structure of KLE-templated $NiFe_2O_4$ and the fact that the stable critical nucleation size of the trevorite crystallites is less than 10 nm.

The present work further establishes the benefits of combining a mesoporous morphology with nanocrystalline films to achieve reasonable levels of facile pseudocapacitive charge storage. While the materials studied here do not break records for high levels of either energy or power density, our results offer insight into how nanoscale porosity can be used to enhance charge storage of a material that shows unfavorable kinetics in bulk form.

Apart from electrochemical charge storage, such KLE-templated $NiFe_2O_4$ thin films could serve as exciting materials for host−guest applications. It is envisioned that the pore-solid architecture of these nanocrystalline samples will facilitate the formation of novel exchange coupled composite materials, which could pave the way for innovative device design. A study of the magnetic properties is currently ongoing.

Acknowledgment. This work was supported by the Fonds der Chemischen Industrie through a Liebig fellowship (T.B.). The authors would like to thank Kirstin Brezesinski, Christian Reitz, Anneliese Heilig, Stephan V. Roth, Jan Perlich, Bruno K. Meyer, Christoph Weidmann, Ken-ichi Iimura, and Alexander Rein for their assistance in materials preparation and measurements. Portions of this research were carried out at the German synchrotron radiation facility HASYLAB/DESY.

Supporting Information Available: Low-magnification SEM, TEM, and AFM images. SAXS data in Bragg−Brentano geometry. Cyclic voltammetric data comparing Li^+ and TBA^+ electrolytes. This material is available free of charge via the Internet at http://pubs.acs.org.